Classification of Arctic Sea Ice Surface Types During the Melt Season in High Resolution IceBridge Imagery

Ellen Buckley

A scholarly paper in partial fulfillment of the requirements for the degree of
Master of Science
May 2019

Department of Atmospheric and Oceanic Science, University of Maryland
College Park, Maryland

Advisor: Dr. Sinéad Farrell

Project Coauthors:

Sinéad L. Farrell: Earth System Science Interdisciplinary Center, University of Maryland, College Park, MD.; NOAA Laboratory for Satellite Altimetry, College Park, MD. sinead.farrell@noaa.gov

Kyle Duncan: Earth System Science Interdisciplinary Center, University of Maryland, College Park, MD.; NOAA Laboratory for Satellite Altimetry, College Park, MD. kyle.duncan@noaa.gov

Laurence N. Connor: NOAA Laboratory for Satellite Altimetry, College Park, MD. laurence.connor@noaa.gov

John M. Kuhn: NOAA Laboratory for Satellite Altimetry, College Park, MD. john.m.kuhn@noaa.gov

Roseanne T. Dominguez: Universities Space Research Association; NASA Ames Research Center, Moffett Field, CA. roseanne.dominguez@nasa.gov

Table of Contents

Abstract

Melt ponds play an important role in the summer evolution of Arctic sea ice. Ponds reduce the albedo of the surface, allowing for increased solar energy absorption and thus further melting of snow and ice. Analyzing the spatial distribution and temporal evolution of melt ponds helps us understand the sea ice processes that occur during the summer melt season. It has been shown that the inclusion of melt pond parameters in sea ice models increases the skill of predicting the summer sea ice minimum extent. Previous studies have used remote sensing imagery to characterize surface features and calculate melt pond statistics. Here we use new observations of melt ponds obtained by the Digital Mapping System (DMS) flown onboard NASA Operation IceBridge (OIB) during two Arctic summer melt campaigns which surveyed thousands of kilometers of sea ice and resulted in the collection of more than 45,000 images. We have developed a pixel-based classification scheme by considering the different RGB spectral values associated with each surface type. We identify four sea ice surface types: undeformed ice, deformed ice, melt ponds, and open water. The classification scheme enables the calculation of melt pond fraction and ice concentration. We evaluate the success of the methodology by analyzing the classification results for a flight on 24 July, 2017 in the Lincoln Sea, north of Greenland. We find that melt pond fraction ranged from 0 to 0.56 along the flight line and the mean is 0.19. Ice concentration values ranged from 2 % to 100 %, with an average concentration of 90.2 %. These values compare favorably with the AMSR2-derived ice concentration, although this study demonstrates the limitations of low-resolution satellite-derived sea ice concentration. Future work involves applying our methodology to the remainder of the DMS dataset to derive high-resolution, Arctic-wide sea ice surface melt parameters, that may be used to improve melt pond parameterizations in sea ice models.

Acknowledgements

I am deeply grateful to my primary advisor Dr. Sinéad Farrell for her conception of this project, guidance throughout my research, support of collaboration with others, meticulous editing, and enduring patience. I am also appreciative for my academic advisor Dr. Jim Carton for his support and guidance with my academic endeavors.

I am thankful for the work space and resources provided by the Laboratory for Satellite Altimetry (LSA) at the National Oceanic and Atmospheric Administration (NOAA) Center for Weather and Climate Prediction. This collaboration with NOAA is possible through the Cooperative Institute for Climate & Satellites-Maryland through the Earth System Science Interdisciplinary Center at the University of Maryland. Many thanks to my collaborators at LSA: Kyle Duncan, Larry Connor, and John Kuhn for answering endless questions and providing feedback. Thanks to my collaborator Roseanne Dominguez, the Digital Mapping System lead instrument engineer.

This project was funded by the NASA Cryosphere Program Grant 80NSSC17K0006.

List of Tables

List of Figures

Chapter 1: Introduction

1.1 Arctic Sea Ice

Arctic sea ice plays an important role in the Earth's climate system: it controls heat (Maykut 1978) and moisture (Screen and Simmonds 2010) fluxes between the atmosphere and ocean, and reduces the amount of solar energy absorbed by the ocean (Curry et al. 1995). The extent of sea ice, and intensity of heat and moisture flux in the Arctic, influence the strength of the jet stream, affecting mid-latitude weather (Francis and Vavrus 2015). The formation of sea ice results in an input of dense, saline water into the surface layer of the ocean that sinks through the water column, driving the thermohaline circulation (Clark et al. 2002). In addition, sea ice provides habitat for marine animal and biological activity (Osborne et al. 2018), and has socio-economic importance as the extent of sea ice determines the navigability of the Arctic Ocean (Perovich 2011).

The 40-year record of satellite observations of Arctic sea ice extent (Fetterer et al. 2017) reveals a negative trend in every month for the time period 1979- 2018 with the most negative trend observed in September (-14%), the month during which the sea ice reaches its annual minimum extent (Osborne et al. 2018). There is also evidence that the rate of September sea ice loss is accelerating (Comiso et al. 2008). Furthermore, the sea ice is transitioning from thick multiyear ice to a predominantly younger (Comiso 2012), and thinner (Kwok and Rothrock 2009; Laxon et al. 2013) ice cover.

1.2 Melt Ponds on Sea Ice

Given the transformation underway in the Arctic, it is essential to understand the factors driving the change in the ice cover so that we may better predict future conditions. During the summer, melting of snow on sea ice results in the formation of melt ponds in the low-lying topography of the sea ice (Polashenski et al. 2012). The topographic relief of the sea ice surface determines the spread of meltwater across the surface (Polashenski et al. 2012). For this reason, melt ponds manifest differently on first year ice and multiyear ice, as illustrated in Figure 1.

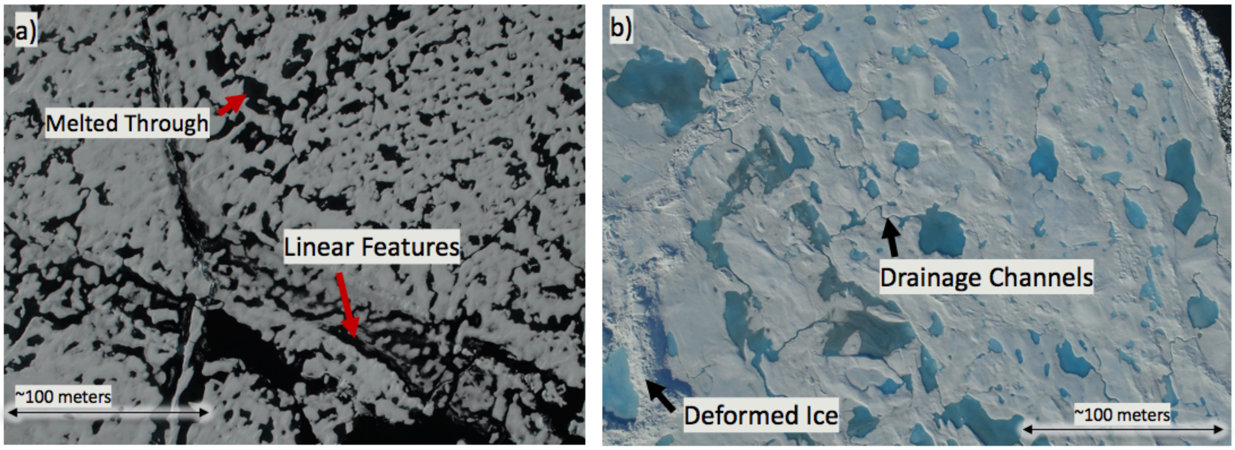

Figure 1. *High resolution visible band airborne imagery of melt ponds (a) first year sea ice in the Beaufort Sea in July, 2016 and (b) multiyear sea ice north of Ellesmere Island in July, 2017. Both images show melt ponds late in the melt season: the first-year ice melt ponds have melted through the ice (a), while the multiyear ice ponds have formed drainage channels (b).*

First year ice, ice having only experienced one growth season (WMO 1970), is now the most prominent ice type in the Arctic (Perovich et al., 2018) and is especially prevalent in the peripheral seas, outlying the central Arctic Ocean Basin. First year ice has a low topographic relief due to its short history of deformation, allowing snow to drift across level ice surfaces unobstructed, resulting in a less variable snow distribution (Petrich et al. 2012; Webster et al. 2015). On thin, first year ice, the melt pond area increases throughout the season because the flat topography allows for the melt ponds to expand horizontally (Grenfell and Perovich 2004). The ability of ponds to grow laterally on first year ice can lead to the melt out of thin ice by the end of the melt season (Fetterer and Untersteiner 1998) (Figure 1a).

Multiyear ice, defined here as ice that has survived at least one summer melt season and includes second-year ice (WMO, 1970), is predominantly found in the Arctic Ocean Basin north of Greenland and the Canadian Archipelago. It is deformed prior to the melt season from collisions of sea ice floes forming pressure ridges which act as obstacles for drifting snow

(Eicken et al. 2004; Petrich et al. 2012) (Figure 1b). Compared with first year ice, the topography of multiyear ice is undulating, thus limiting the lateral spread of melt ponds across the surface. On multiyear ice, ponds are confined to low-lying areas in deep pools (Polashenski et al. 2012). Following the peak areal coverage of melt ponds, melt water drains through drainage channels and pores that develop in the ice, resulting in a decreasing pond area (Fetterer and Untersteiner 1998), a decrease that has been observed to be more significant on first year ice than on multiyear ice (Polashenski et al. 2012).

Since melt ponds have a lower albedo than the surrounding sea ice, this allows for additional heat uptake and further ice melting (a positive feedback, Curry et al. 1995). The melt pond albedo depends on the depth of the pond and the thickness of the underlying ice (e.g., Lu et al. 2018). Melt pond albedo for dark melt ponds typically found on thin first year ice is less than 0.2, and around 0.35 for light ponds found on multiyear ice (Perovich 2017). As the sea ice melts away, the open ocean is exposed, replacing one of the highest albedo surfaces on Earth (snow-covered sea ice, albedo greater than 0.8) with one of the lowest albedo surfaces (open ocean, albedo less than 0.1) (Perovich and Polashenski 2012; Perovich 2017). Melt ponds also increase the transmission of light through the ice, allowing for blooms of under-ice phytoplankton (Arrigo et al. 2012). In contrast with the surrounding frozen sea ice surface, melt ponds provide a source of moisture to the atmosphere and intensify the surface turbulent momentum transfer (Boisvert et al. 2013). Additionally, the appearance of melt ponds on the sea ice surface provide us with information on the timing of summer melt, the amount and distribution of snow, and the topography of the sea ice (Fetterer and Untersteiner 1998).

Melt ponds are difficult to measure for a number of reasons. The harsh Arctic environment and dangerous ice conditions make an unfavorable situation for conducting large-scale in situ studies. The prevalence of low-lying clouds in the Arctic, especially in the summer

(Intrieri et al. 2002), can obstruct remote sensing measurements from space. In passive remote sensing techniques, melt ponds and open water have similar infrared emissions (Fetterer and Untersteiner 1998) so it is difficult to distinguish between ponded and open water. Perhaps the most prohibitive characteristic for measuring melt ponds is their small size (on the order of 10 m^2) (Perovich et al. 2002b), requiring high-resolution observations that resolve the individual melt pond details. In situ studies can provide us with detailed information about the small-scale features of summer sea ice. For example, the Surface Heat Budget of the Arctic Ocean program (SHEBA), was a drifting ice camp in the Beaufort Sea from October 1997 to October 1998 (Uttal et al. 2002). It advanced the understanding of melt pond albedo (Perovich et al. 2002a), melt pond fraction and size distribution (Perovich et al. 2002b) and improved modeling efforts (Curry et al. 2001). However, in situ studies are limited in spatial and temporal extent.

Airborne and remote sensing offers the potential for Arctic-wide melt pond observations. Previous studies have demonstrated the ability to extract sea ice melt pond parameters from airborne (Tschudi et al. 2001; Miao et al. 2015; Wright and Polashenski 2018) and satellite imagery (Rösel and Kaleschke 2011; Tschudi et al. 2008; Rösel et al. 2012; Markus et al. 2002; Markus et al. 2003; Fetterer and Untersteiner 1998; Webster et al. 2015; Zege et al. 2015; Istomina et al. 2015; Mäkynen et al. 2014). However, these studies were limited by both the spatial resolution and aerial coverage of the observations. Some studies were limited to small regions of the Arctic; Miao et al. (2015), Webster et al. (2015), Tschudi et al. (2001), and Fetterer and Untersteiner (1998) were all limited to the Beaufort and Eastern Chukchi Seas. Others were limited by low pixel resolution of the satellite data from the Moderate Resolution Imaging Spectroradiometer (MODIS) with 12.5 km resolution (e.g. Rösel and Kaleschke 2011; Tschudi et al. 2008; Rösel et al. 2012), Medium Resolution Imaging Spectrometer with1 km resolution (e.g., Zege et al. 2015; Istomina et al. 2015), ENVISAT wide-swath mode synthetic aperture radar images (WSM SAR) with 120 m resolution (Mäkynen et al. 2014), and Landsat Enhanced Thematic Mapper (ETM+) images with 30 m resolution (e.g. Markus et al. 2002; Markus et al. 2003). Due to the pervasive cloud cover in the Arctic in the summer, much of the data must be discarded in satellite data analysis. Some studies found the availability of useable data was minimal (e.g., Rösel and Kaleschke 2011). Because of these limitations, gaps remain in our knowledge of melt pond areal coverage, size, and distribution at an Arctic-wide level.

1.3 Classification of Sea Ice Surface Features in High-Resolution Imagery

It is essential to study melt pond properties and processes in order to represent them in climate models and understand their role in summer sea ice evolution. It has been shown that sea ice models are very sensitive to melt pond inclusion (Flocco et al. 2010), and that the inclusion of melt ponds improves sea ice models, resulting in better predictions of the end of melt season ice extent (by 13%) and ice volume (by 40%) (Flocco et al. 2012), and spring melt pond area can be used to predict the summer minimum extent (Schröder et al. 20014). Currently, a common method of incorporating melt ponds into sea ice models is by simply decreasing the overall sea ice albedo in the summer months (Hunke et al. 2010). However, this does not take into account the regional ice type and topography, or the natural variability of melt pond areal fraction and range of albedos (Flocco et al. 2012). This motivates our work to investigate the features of melt ponds on sea ice using remote sensing, so as to improve our understanding of summer sea ice melt processes and melt pond properties. Ultimately, these new observations may be incorporated into sea ice models to further improve predictive capabilities.

In this study we use new observations of melt ponds on Arctic sea ice, obtained during the NASA Operation IceBridge (OIB) airborne missions conducted in two summer melt seasons. A total of eleven sea ice surveys were flown, during which data were collected over a total of approximately nine thousand kilometers, resulting in more than 45,000 images of sea ice undergoing melt (Dominguez 2010). One campaign was conducted from July 16 - 21, 2016, and surveyed sea ice in the Beaufort and Chukchi Seas. A second campaign was conducted from July 17 - 25, 2017, and surveyed ice in the Lincoln Sea and the Arctic Ocean north of Greenland and Canada. We utilize the high-resolution imagery collected by the Digital Mapping System (DMS) flown onboard OIB and develop a pixel-based classification scheme to identify four sea ice surface types: undeformed ice, deformed ice, open water, and melt ponds. This study acts to test the feasibility of a classification algorithm for high-resolution sea ice imagery. We examine a case study in the Lincoln Sea on July 24, 2017 and analyze the derived melt pond fraction and ice concentration parameters. We plan to expand this work to the entire dataset and work to fill the gaps in our knowledge of small-scale melt season processes by providing high resolution observations of melt ponds across a large region of the Arctic.

Chapter 2 describes the DMS dataset used for sea ice surface classification. Chapter 3 describes the data quality control process, the classification algorithm methodology, and the calculations of melt pond parameters. Chapter 4 is a presentation and discussion of the findings and puts the results into context of existing studies. We also discuss the uncertainties and errors of the data and algorithm in this chapter. The conclusions and ideas for future work are detailed in Chapter 5.

Chapter 2: Data

2.1 NASA Operation IceBridge

The Operation IceBridge mission was designed to fill the data gap between ICESat (decommissioned in 2009) and ICESat-2 (launched in 2018) satellites by collecting detailed surface measurements in the Arctic and Antarctic (Koenig et al. 2010). For the Arctic summer flights of 2016 and 2017 (Figure 2), the NASA 524 HU-25C Guardian, operated at a nominal flight altitude of ~460 m, and was equipped with a suite of instruments (Koenig et al. 2010). Instruments included a snow radar (Panzer et al. 2013), laser altimeter (Krabill et al. 2002), and a digital camera (Dominguez 2010), with positioning capabilities. The coincident datasets collected during this mission allow for a comprehensive investigation of summer sea ice melt processes and properties. The OIB melt campaigns were conducted in different regions of the Arctic exploring distinct ice regimes. A comparison of the two campaigns is detailed in Table 1.

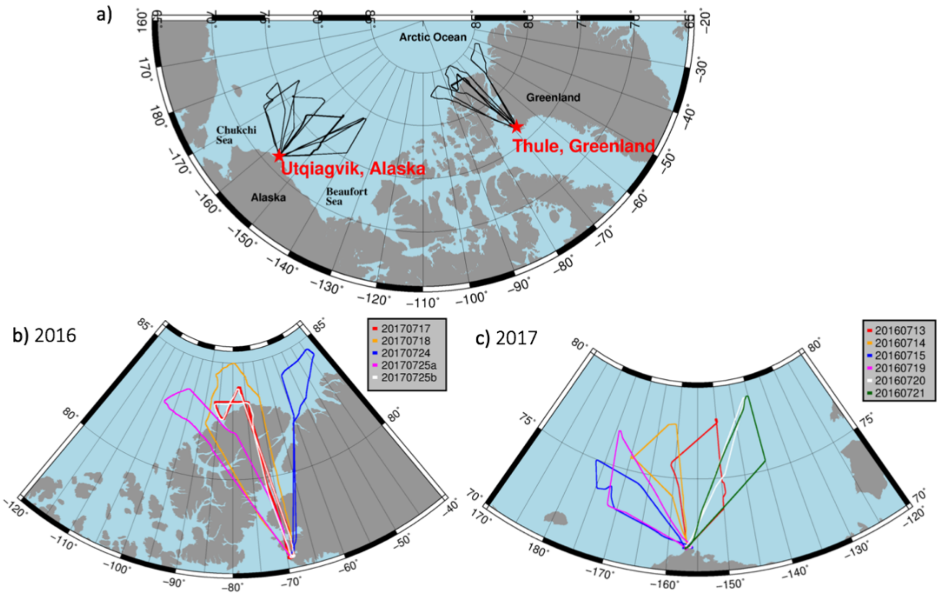

Figure 2. *Operation IceBridge Arctic summer flight paths. a) The Arctic summer flights based from Utiqiagvik (Barrow), Alaska and Thule, Greenland. b) The 2016 Arctic summer flights based from Utqiagvik, Alaska over the Beaufort and Chukchi Seas. c) The 2017 Arctic summer flights based from Thule, Greenland over the Lincoln Sea and Arctic Ocean, north of Ellesmere Island.*

Table 1. Summary of DMS image data collection during OIB Arctic Summer campaigns

	Arctic Summer Melt 2016	**Arctic Summer Melt 2017**
Dates	13-21 July 2016	17-25 July 2017
Base airport	Utqiagvik (Barrow), Alaska	Thule, Greenland
Location of data collection	Chukchi Sea & Beaufort Sea	Arctic Ocean & Lincoln Sea
# of sea ice flights	5	6
# of images collected	20,559	25,610
Total area photographed	~ 2350 km^2	~ 2950 km^2
Ice type (Haas 2017)	First year and mixed	Multiyear
Mean winter sea ice thickness (Haas 2017)	1-2.5 m	3-6 m

The OIB 2016 campaign includes overflights of moorings, two CryoSat-2 underflights, and specific excursions to measure multiyear ice and first year ice and to test the range limit of the aircraft. The OIB 2017 campaign includes a flight to measure the thickness of the ice and ridge heights, and an attempted repeat track of this flight one week later to study changes. Other flights were designed to overfly areas flown during the OIB Arctic spring 2017 campaign, and to measure ice advected from the spring CryoVEx mission. (Studinger et al. 2011). The 2017 campaign was flown over the thickest and oldest ice in the Arctic, to the north of Canada and Greenland, where the Transpolar Drift pushes ice against the coast causing dynamic thickening (Haas 2017). The 2016 campaign measures ice in the Beaufort and Chukchi seas where the magnitude of convergence against the coast is not as great, and much of the ice does not survive the summer melt season, resulting a thinner and younger ice cover.

2.1.1 Digital Mapping System

This study utilizes the IceBridge DMS L1B Geolocated and Orthorectified Images (Dominguez 2010). The Digital Mapping System (DMS) captured images every 5 seconds. At the nominal flight altitude, each image covers a surface area of ~ 575 m x ~ 400 m. Each DMS image comprises a geotiff array with a black border surrounding the surface pixels. Each pixel within the image has a resolution of 0.1m and an associated red, green, and blue channel value (RGB data) (Dominguez 2010). The corrected Position and Attitude Data (PAD) collected by the Applanix 510 POS AV system flown with the DMS provides aircraft parameters that have been used to apply orthorectification and geolocation to all of the DMS images (Dominguez 2010). The DMS data are available in jpeg and geotiff formats. We use the jpeg compressed files for quick views of images for quality control and flagging of the corresponding full resolution geotiffs. The geolocated and orthorectified level-1B (IODMS1B) DMS geotiff data are used in the feature classification steps. Previously, DMS data have been used for lead detection (Farrell et al. 2011; Onana et al. 2012), pressure ridge sail height measurements (Duncan et al. 2018), characterization of sea ice surface morphology (Newman et al. 2014), and roughness (Webster et al. 2015). Here, we take advantage of the high-resolution DMS images to classify sea ice surface types including small scale features such as melt ponds and deformed ice. Continuous sampling throughout the flights allows for calculation of along-track parameters such as ice concentration and melt pond fraction.

Chapter 3: Methodology

Our goal is to classify DMS surface pixels into four categories: undeformed ice, deformed ice, open water and melt pond (Figure 4). The DMS images are not routinely adjusted for scene brightness due to varying overhead cloud conditions and sun angle, and are thus not uniformly lit. Therefore, it is essential that surface type classification criteria are not based on fixed thresholds. Rather, criteria are applied on a per image basis, and automatically adjust to suit the specific brightness levels of each image. We utilize the red, green and blue channels of each DMS image (Cr, Cg, Cb), and the normalized pixel value, Cn, defined in Equation 1:

$$Cn = (Cr - Cg)/(Cr + Cg) \tag{1}$$

We analyze histograms of the pixel distribution in these channels using a bin width of 2 pixel values for the Cr, Cg, and Cb, and 0.02 for Cn, to ensure high resolution and to more easily visualize the underlying frequency distribution. Modes are defined as a collection of bins bounded by pixel count minima on either side. The modal values of the histogram modes are defined as bins with lower pixel count on either side. The difference between pixel count must be greater than 0.05% of the total number of pixels counted in the histogram so that erroneous modes are not detected. The maxima (ma) are annotated as follows: Cx_ma_y where x is r (red), g (green), b (blue), or n (normalized) and y is the mode number, counting from 1, the modal value with the lowest pixel values, to m, the modal value with the highest pixel values. For example, the second mode in Cr is labeled Cr_ma_2. Similarly, the minima (mi) are defined as a bin with higher pixel counts on either side and are labeled Cx_mi_y. We also utilize the half maximum (hm) and quarter maximum (qm) of the mode on the left (L) or right (R) side of the mode. The half (quarter) maximum is the bin at which the pixel count is equal to 0.5 (0.25) of the pixel count in the associated mode. E.g., to denote the half maximum bin value on the left side of the second mode in the blue channel, we write Cb_ma_2_hmL. Figure 3 shows an example Cr histogram with meaningful statistical values labeled.

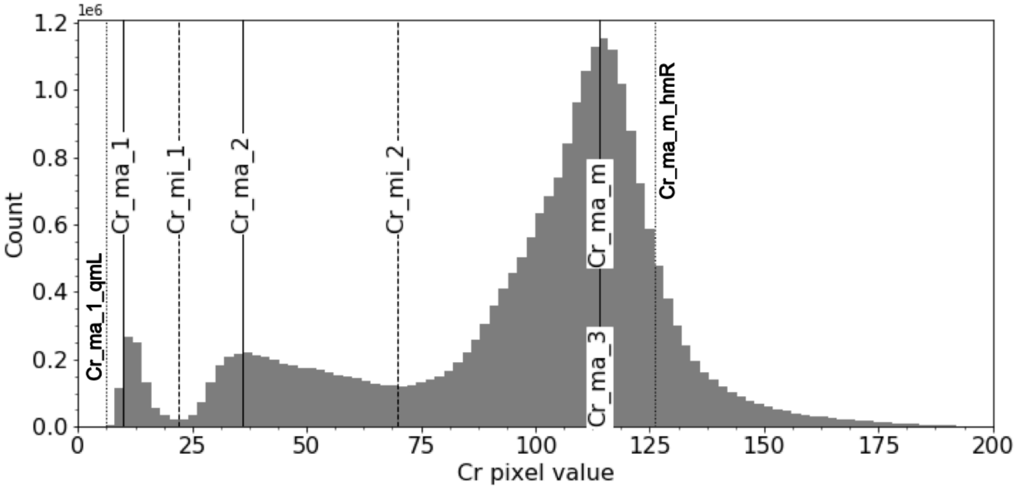

Figure 3. *Example Cr histogram with statistical values labeled. Cr_mi_ denotes minima numbered 1-2. Cr_ma_ denotes modal values numbered 1, 2, and 3, with the highest mode (3) also referred to as Cr_ma_m. The quarter maximum value on the left of the first mode (Cr_ma_1_qmL) is labeled, as well as the half maximum value on the right of the highest pixel value mode (Cr_ma_m_hmR).*

3.1 Data Quality Control

Prior to preprocessing and classification, we perform a data quality assessment to ensure the consistency of our analysis for obtaining robust results. Metadata associated with each image provide image acquisition time, latitude, longitude, pixel size (*ps*), and aircraft pitch (A_p), and roll (A_r). At a nominal flight altitude of 460 m, $A_\mathrm{p} = 0^\circ$ and $A_r = 0^\circ$, $ps = 0.1$ m. We retain only those images acquired under nominal flight conditions, eliminating any images collected during aircraft maneuvers. We limit our study to DMS images with $ps < 0.25$m, and A_r, $A_p < \pm 5$ degrees. These filtering steps ensure that each pixel represents a consistent surface area, simplifying calculations of the area of each sea ice parameter derived from the classified pixels. In addition, images containing clouds and land are manually removed from the data set by visual inspection: Each DMS jpeg is individually inspected and flagged for obstructions that obscure the surface, e.g. clouds. We also flag images of land surfaces, since the algorithm is designed for classification of ocean and sea ice features only. Flagged images are removed from the data set.

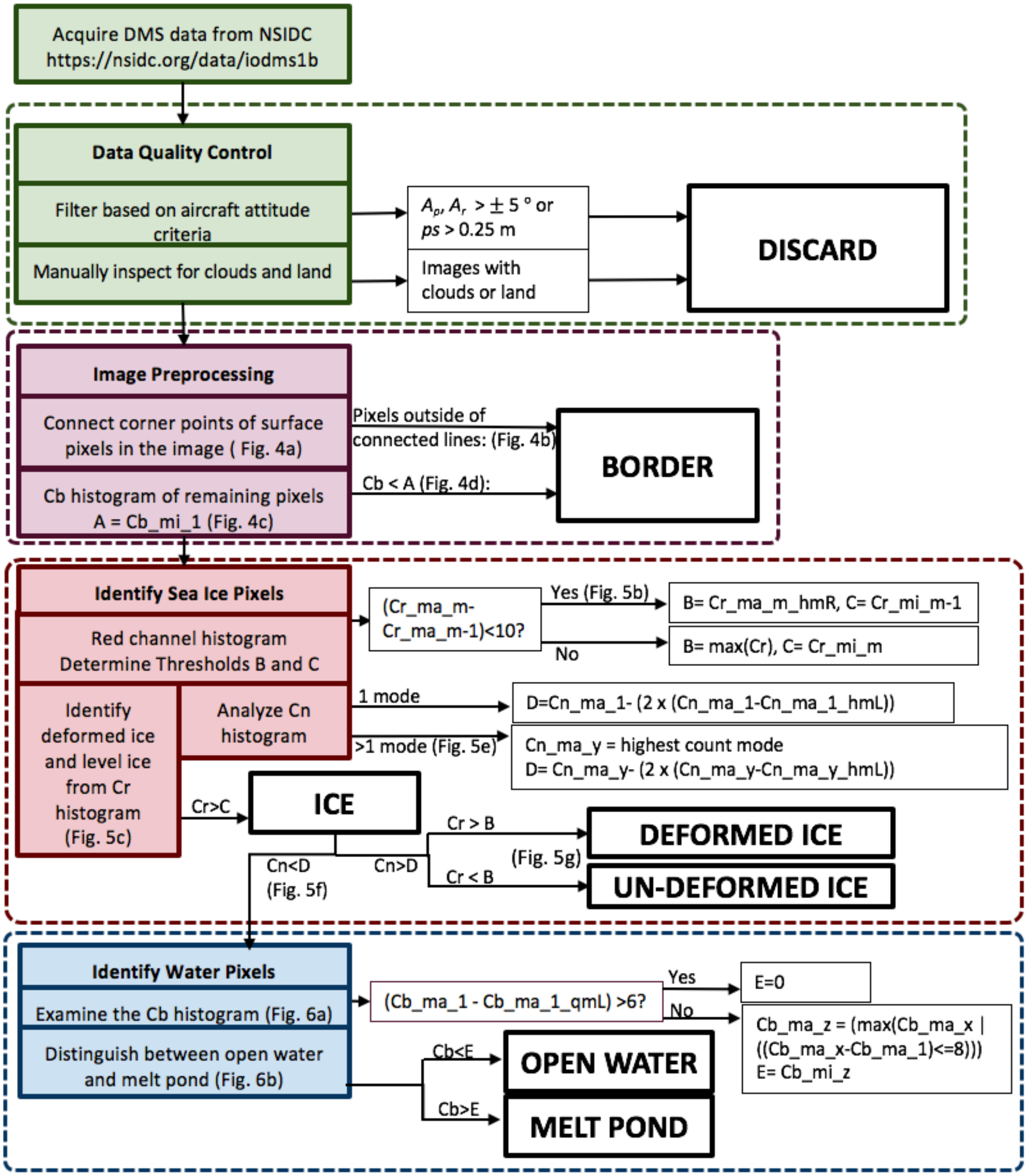

Figure 4. *A schematic detailing the surface classification algorithm including steps to identify deformed ice, undeformed ice, open water and melt pond pixels. Corresponding images are noted where applicable. The notation "|" here is used to mean "such that." Here, the colored boxes generalize the steps with the equations to describe specific conditions and thresholds set for each classification step. The green indicates the data quality control step (Section 3.1), the purple indicates the image preprocessing step (Section 3.2) and the red then blue indicates steps of the classification algorithm (Section 3.3.1, 3.3.2) The final products are indicated by white boxes with thick black outlines.*

3.2 Image Preprocessing

The DMS image pixels include the black border pixels, surrounding the surface pixels. The number of black border pixels is variable between images in the dataset, as it is used to mitigate the effects of the varying aircraft pitch, roll, and altitude on the resulting shape of the image projected to the Earth's surface. As a first preprocessing step, it is necessary to identify and eliminate border pixels in each geotiff so that we analyze only the surface pixels that are associated with the sea ice and ocean surface. We identify corner points of the image as the first pixel from each direction with Cr > 4 (Figure 5a). Pixels outside of the lines connecting these corner points are identified as border and discarded. Due to the georeferencing of the images, even after the first step, some border pixels remain within these lines and still require identification (Figure 5b). We examine a histogram of the remaining pixels (Figure 5c) and eliminate pixels < Cb_mi_1 (Figure 5d). The remaining pixels are the surface pixels.

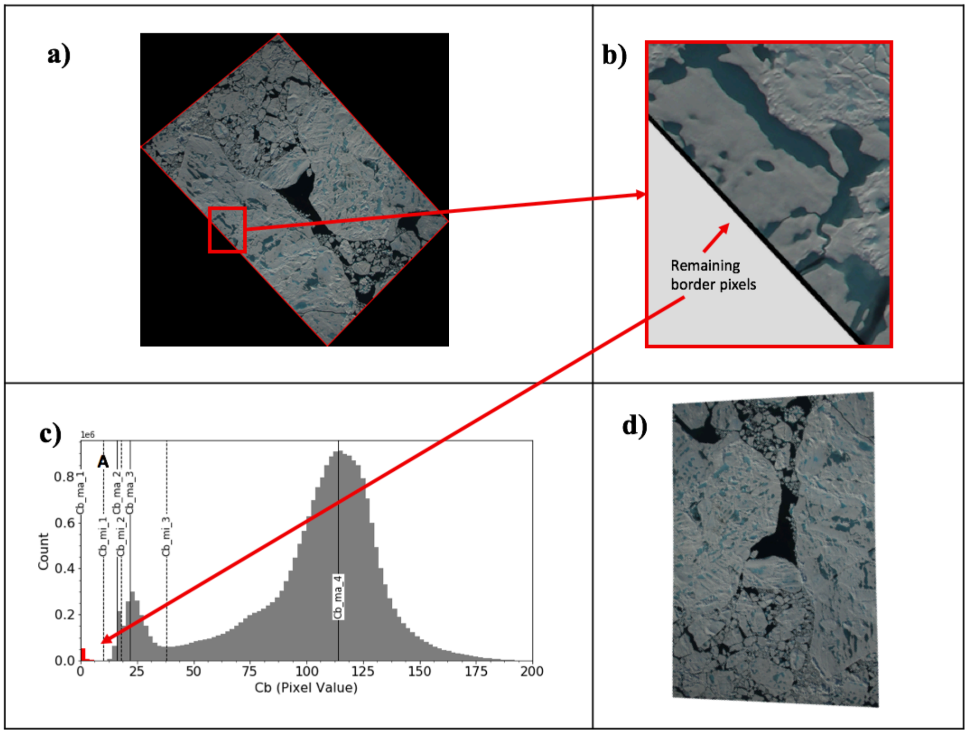

Figure 5. *Series of figures describing the methodology used to identify DMS border pixels. (a) original image with the corner points connected. (b) unclassified border pixels after the first step. (c) where these remaining pixels reside on the blue histogram. (d) rotated image with all border pixels identified and removed.*

3.3 Feature Classification

After filtering and preprocessing the data, surface pixels within each DMS image are classified as deformed ice, undeformed ice, open water, and ponded ice. Each of the four classes identified in these images has a unique signature in the three color channels and therefore it is feasible to classify individual pixels based on the RGB values relative to other pixels in the image.

3.3.1 Sea Ice

Snow-covered sea ice has high RGB values that are similar in all three channels resulting in the bright neutral-colored white surface. When ice floes collide, the ice is deformed, creating pressure ridges and breaking into blocks. Here we define deformed ice as any rubbled or ridged ice. Some faces of the blocks of broken ice are oriented towards the sun resulting in the brightest surface relative to all other surface pixels.

In the Cr histogram, the ice pixels occupy the highest bins and form a distinct mode, Cr_ma_m. In some images with significant amounts of deformed sea ice, there are two high value modes in the red channel histogram (Cr_ma_m and Cr_ma_m-1). If deformed ice is present, the highest value modes in the red channel are within 10 bins of each other ((Cr_ma_m – Cr_ma_m-1) <10) and both modes are associated with ice pixels (Figure 6b). In this case, Threshold B is defined as the first bin to the right of Cr_ma_m that is less than half of the pixel count in the modal value bin (Cr_ma_m_hmR) (Figure 6b):

$$B = Cr\_ma\_m\_hmR \tag{2}$$

Threshold C is set as the minimum before the second highest mode (Figure 6b):

$$C = Cr\_mi\_m - 1 \tag{3}$$

In the case of no deformed ice, where ((Cr_ma_m – Cr_ma_m-1) >10), Threshold B is set as the maximum pixel value in the red channel and Threshold C is defined as:

$$B = \max(Cr) \tag{4}$$

$$C = Cr\_mi\_m \tag{5}$$

After setting the threshold depending on the presence of deformed ice, we classify ice pixels (ICE):

$$\boldsymbol{ICE\ are\ defined\ as}: \boldsymbol{Cr \geq C}$$

$$\boldsymbol{Deformed\ pixels\ are\ defined\ as}: \boldsymbol{Cr \geq B}$$

$$\boldsymbol{Undeformed\ ice\ pixels\ are\ defined\ as}: \boldsymbol{C\ \leq Cr < B}$$

In these steps some melt pond pixels are misclassified as ice (Figure 6c, 6d). These misclassified pixels are located in the lightest melt ponds, i.e., shallow ponds with thick ice draft below. To separate the melt pond pixels from the ice pixels, we introduce another requirement to refine the ice mask. Melt ponds have high green and blue channel values compared to the red channel values. We look at the histogram of normalized pixel value (Cn). Melt pond pixels have lower normalized values than ice pixels. If there is only one mode, Threshold D is set as the mode minus two times the distance from the mode to the half max on the left:

$$D\ =\ Cn\_ma\_1 - (2 \times\ (Cn\_ma\_1 - Cn\_ma\_1\_hmL\ )) \tag{6}$$

Similarly, if there is more than one mode (Figure 6e), we identify the mode that has the highest pixel count (i.e. the location of the maximum Cn bin):

$$Cn\_ma\_y\ = highest\ pixel\ count\ mode \tag{7}$$

Where y is 1, 2, 3…, m-1, m in the Cn histogram. In this case, Threshold D is set as the highest pixel value minimum with a lower pixel value than the identified mode (Figure 6c):

$$D = Cn\_mi\_y - 1 \tag{8}$$

All pixels with a normalized value less than Threshold D are classified as light melt ponds (MP_L) and removed from the ice mask (Figure 6d).

$$\boldsymbol{MP_L\ are\ defined\ as}\ (\boldsymbol{Cn < D})\ \&\ (\boldsymbol{Cr \geq C})$$

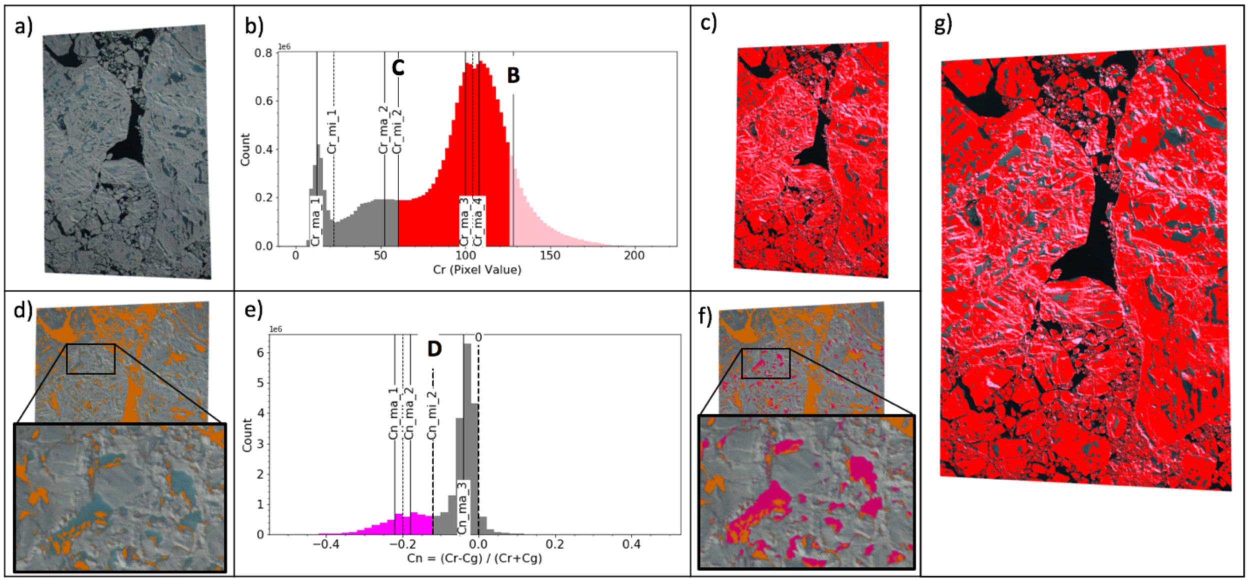

Figure 6. *Series of figures describing the methodology used to identify DMS ice pixels. (a) the image with no border (after preprocessing). (b) the red histogram (Cr) of the remaining pixels. Here thresholds are identified to separate the deformed ice and undeformed ice. (c) undeformed ice pixels are red, deformed ice pixels are pink. (d) classified ice pixels shown in natural color, not classified as ice pixels shown in orange. This is a demonstration of the misclassification of light melt pond pixels as ice pixels. (e) histogram of the normalized pixel value remaining after border preprocessing (Cn). Pixels less than Threshold D are colored in pink. (f) pixels not classified as ice in first step in orange, additional pixels removed from the ice mask in pink, pixels classified as ice as natural color.*

3.3.2 Water

The two water classes, melt pond (MP) and open water (OW), are in some cases difficult to distinguish and define. Here, we define melt ponds as ponded freshwater on the sea ice surface. As soon as the ponded water melts through the ice and exposes the open ocean, it is considered open water since those have the same pixel values as open water in all channels. Open water has the lowest value in all channels in these images. Open water is found in the leads between ice floes, in melt ponds that have completely melted through the ice, and beyond the ice edge.

Melt ponds range from a light blue to dark blue. The color of the pond depends on the depth of the pond and the properties of the underlying ice (Eicken et al. 2004). Lighter ponds tend to have thick ice below and as the depth increases, the color darkens. Due to the requirement of thick ice below, the lightest melt ponds are more common on thick, multiyear ice than thinner, first-year ice. Melt ponds have high values of Cb and Cg, relative to Cr. The magnitude of these values ranges significantly depending on how light or dark the pond is.

For detecting open water, we use the blue channel, Cb (Figure 7a). If present, open water pixels occupy the lowest value pixels in the blue channel (Cb_ma_1) and form a distinct narrow mode. If the quarter maximum to the left of the lowest value mode (Cb_ma_1_qmL) is fewer than 6 bins from the lowest value mode, there is open water in the image. In some cases, the open water pixels can occupy two closely-spaced, low-value pixel modes. For all the modes within 8 bins of Cb_ma_1, we define Threshold E as the first minimum with a higher bin value than the highest pixel value mode of these modes (Figure 7a), i.e.,

$$Cb\_ma\_z = \max\left(Cb\_ma\_x \;\middle|\; \left(Cb\_ma\_x < \left(Cb\_ma\_1 - 8\right)\right)\right) \tag{9}$$

$$E = Cb\_mi\_z \tag{10}$$

Where x, z are 1, 2, 3, …, m-1, m in the Cb histogram. The distance of 8 bins between the modes and the first mode, was determined empirically and ensures that the mode selected is a low Cb value. If there is no open water, we define Threshold E = 0 and open water is classified as all the unclassified pixels with blue channel values less than Threshold E (Figure 7a):

$$\boldsymbol{Open\ water\ pixels\ are\ defined\ as\ Cb \leq E}$$

After the ice and open water pixels have been identified; the remaining pixels are identified as melt ponds (Figure 7b).

3.4 Calculating Sea Ice Parameters

After the classification of sea ice surface type for each individual surface pixel, we derive meaningful statistics from these results. A number of different sea ice parameters may be calculated by taking the ratio of classified surface pixels. The parameters are calculated on a per image basis and thus, the resolution of the parameters is the total surface area coverage of a DMS image (~400 m x ~575 m, ~0.23 km^2).

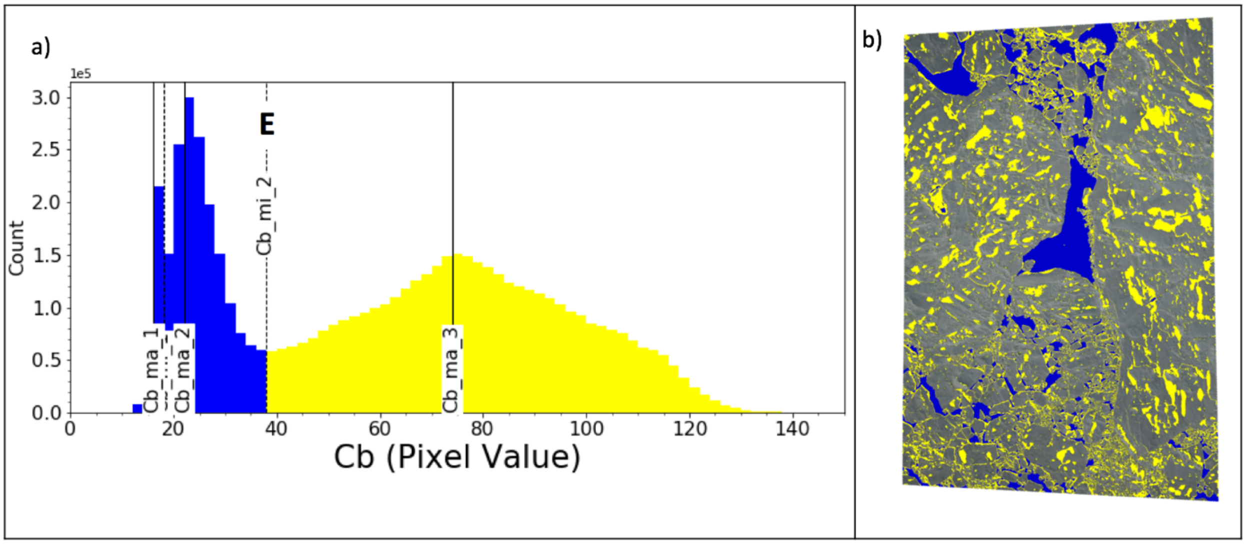

Figure 7. *Methodology used to identify open water pixels. (a) histogram of Cb pixels remaining after ice pixels have been classified. Threshold E separates the blue open water pixels and yellow melt pond pixels. (b) open water pixels in blue, melt pond pixels in yellow, ice pixels in natural color.*

3.4.1 Sea Ice Concentration

After WMO (1970), sea ice concentration (SIC) is defined as “the amount of the sea surface covered by ice as a fraction of the whole area being considered.” Here, we calculate the percentage and define sea ice concentration as:

$$SIC = (MP + ICE)/(MP + ICE + OW) \times 100 \tag{11}$$

3.4.2 Melt Pond Fraction

Melt pond fraction, MPF, is ponded area over the sea ice area (Webster et al. 2015). Here, we define the melt pond fraction as the areal fraction of melt pond pixels on sea ice:

$$MPF = (MP)/(MP + ICE) \tag{12}$$

Chapter 4: Results

In this study we apply the data quality control methods described in Chapter 3.1 to all 46,168 available DMS images collected on the eleven OIB summer Arctic campaigns (Chapter 4.1). To test the capability of the classification algorithm described in Chapters 3.2 and 3.3, we apply the processing steps to data collected during the flight on 24 July, 2017. A total of 3,176 images were processed and their pixels classified as undeformed ice, deformed ice, open water and ponded ice. Following steps outlined in Figure 4, we use results derived from data obtained during this flight as a case study and analyze the successes and limitations of the classification of the DMS image pixels.

4.1 Data Quality Control

DMS images from the eleven OIB Arctic sea ice flights were assessed for data quality control (Figure 8). Figures 8a and 8b show the location of the filtered and remaining images for the 2016 and 2017 flights, respectively. It is common for clouds to obscure long sections of flight, eliminating many consecutive images from analysis. Maneuvers used align the aircraft for flight along pre-defined survey lines can result in significant roll and thus images acquired during these maneuvers must be discarded. The aircraft flies at a higher altitude over the land (as seen in Figure 8b over Ellesmere Island, Canada) during transit from the base location to the survey line so as to maximize flight time at the survey line. Figure 8c shows the results of filtering the DMS image dataset.

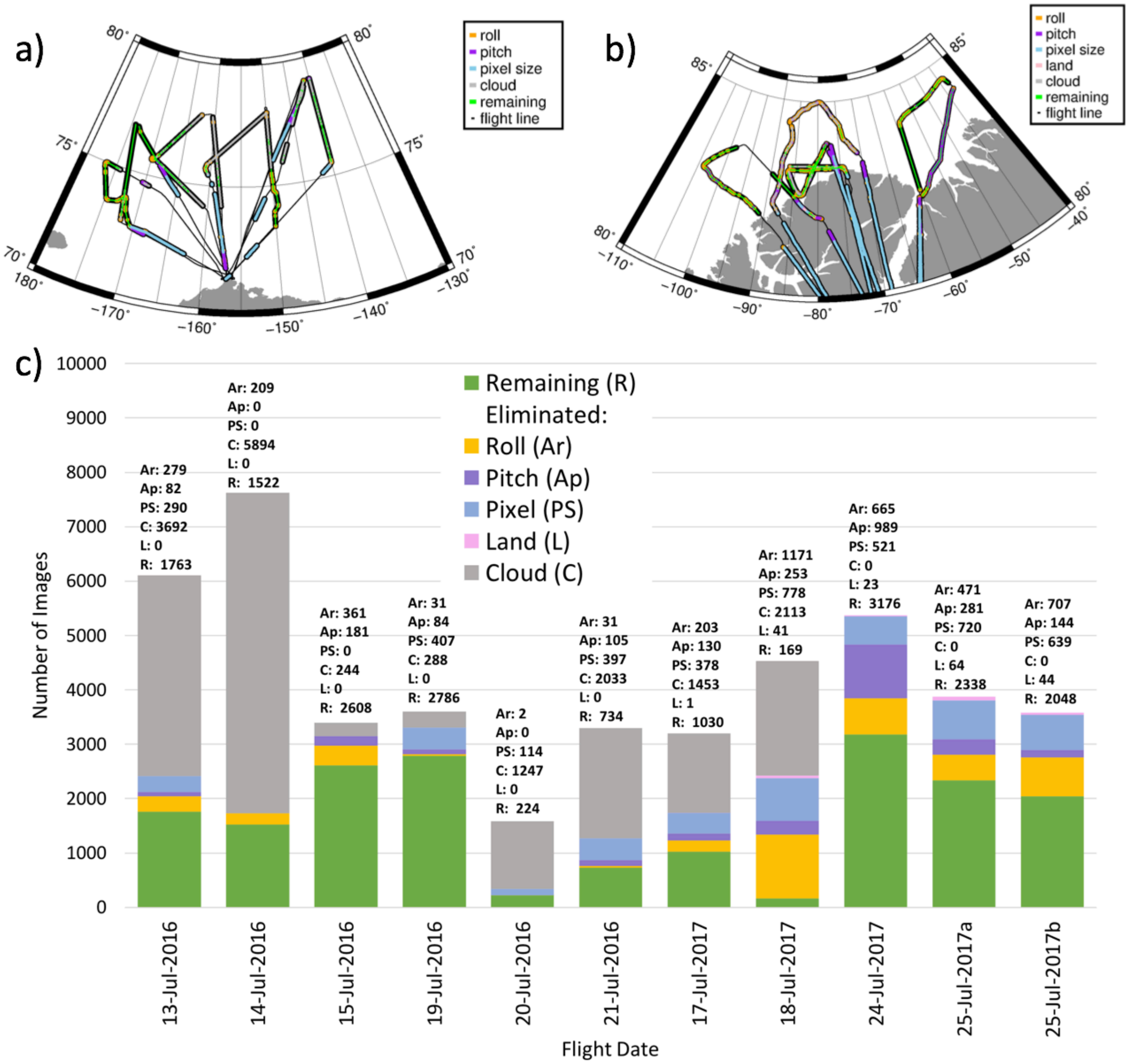

Figure 8. *Maps of summer flights color-coded to indicate the reason for removal and statistics associated with discarded and remaining images for (a) 2016 flights and (b) 2017 flights. (c) Bar graph showing the number of images remaining and discarded for each flight.*

From the 11 flights, 23.1% of the data were removed due to non-nominal aircraft attitude (A_r: 9.0%, A_p: 4.9%, *ps*: 9.2%). A total of 37% of the data were filtered due to clouds obscuring the surface. Less than 1% of images were eliminated due to land. But we note that many of the images containing land were filtered first by the *ps* constraint as the aircraft flies at a higher altitude over land resulting in large pixels outside of the acceptable range. From this quality control step, it is apparent that the 24 July, 2017 flight has the most images remaining in the data set. The flight conditions were excellent, and no data were lost due to clouds (Crittenden 2017). Aircraft maneuvers eliminated 40.9% of the data (A_r: 12.4%, A_p: 18.4%, *ps*: 9.7%). The objective for this survey was to sample the ice in the eastern portion of the aircraft range limit in the Lincoln Sea (Crittenden 2017). We process this one flight to test the success of the algorithm and conduct an in-depth analysis of the classification algorithm results.

In the case of the flight on 24 July, 2017, 3,176 remained after the data quality control step. These were processed using the classification algorithm. Upon inspection of the results, the algorithm failed for 203 images (6.4%). Section 4.5 includes a discussion of why the algorithm was unsuccessful for these images, how the disability to process these images may affect results, and proposed steps to adjust the algorithm in the future.

4.2 Surface Area

Surface area classification was determined for 2,973 images covering approximately 680 km^2. Figure 9 shows the results of the classification algorithm for each image. Gaps in the chart are due to the quality control step. In these areas, the images were removed from the dataset due to aircraft pitch/roll (A_p, A_r), image pixel size (*ps*), or the presence of land. Images 0-300 were eliminated either due to too large of a pixel size, or aircraft pitch, because at this time, the aircraft was flying at a high altitude and approaching the survey line. The large gap between images 2500 and 2600 was due to roll as the aircraft maneuvered to align for another flight leg. There is considerable variability of area coverage throughout the flight. There is a lower percentage of open water pixels towards the beginning of the flight, which was over the areas of greatest sea ice convergence north of Greenland. Towards the end of the flight (images 4700+), there are images with a larger percentage of pixels classified as open water. These are images acquired over the Nares Strait, the channel between Ellesmere Island, Canada, and Greenland, known to be a channel of ice export out of the Arctic (Kwok 2005). Due to ice motion, it is expected that this area has more divergence than the consolidated pack and contains regions of open water. Our results reveal many images with a higher percentage of open water in this region, which is consistent with the known regional ice dynamics.

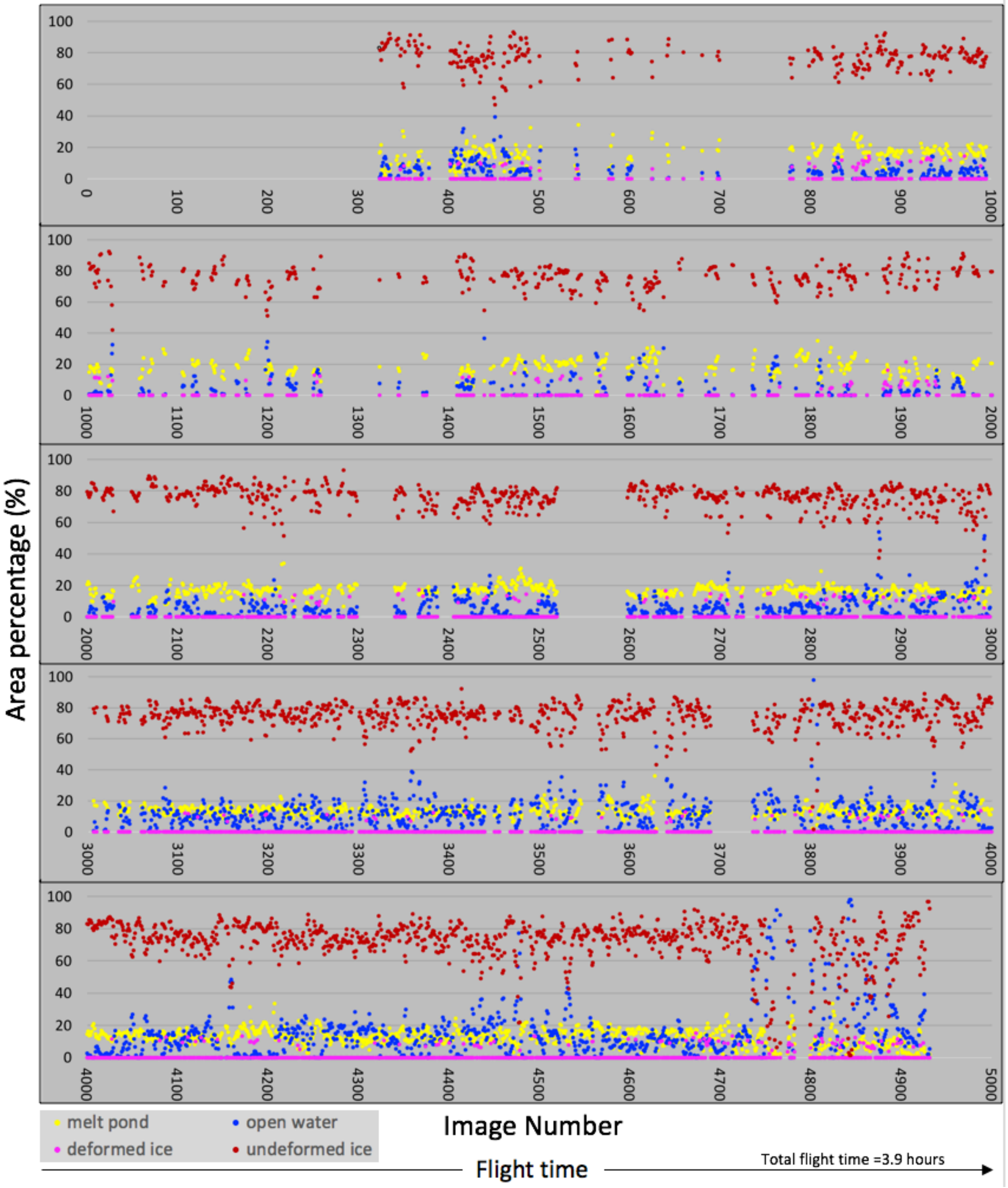

Figure 9. *Area percentage of undeformed ice (red), deformed ice (pink), melt ponds (yellow) and open water (blue) along the survey on 24 July, 2017 in the Lincoln Sea. The image number increases with flight time; total flight time was 3.9 hours.*

4.3 Sea Ice Concentration

From the surface area percentages, we are able to determine SIC. Figure 10 shows the SIC for the data acquired from the survey on 24 July, 2017.

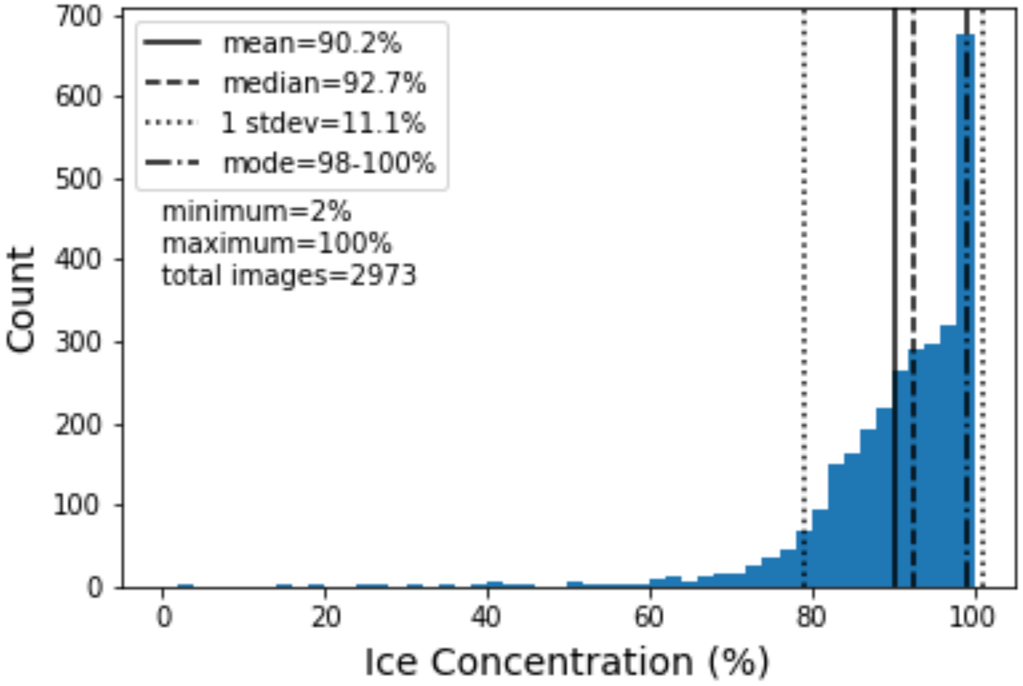

Figure 10. *Histogram of ice concentration percent calculated per image along the survey line flown on 24 July, 2017 over the Lincoln Sea. The bin width is bin width is 2%. The ice concentration resolution is ~400 m x ~575 m (0.23 km^2).*

The median sea ice concentration was 92.7%. The mean was 90.2% with a standard deviation of 11.1%. The ice concentration values range from 2% to 100%. In contrast to the Nares Strait, the Lincoln Sea north of Greenland and the Canadian Archipelago is an area of known ice convergence (Kwok 2015), due to coastal boundaries that restrict ice motion. When ice floes collide, they deform and thicken. Thick ice is more likely to survive the summer melt season, so we expect to see higher values of ice concentration along this flight path in the consolidated ice zone (Figure 11).

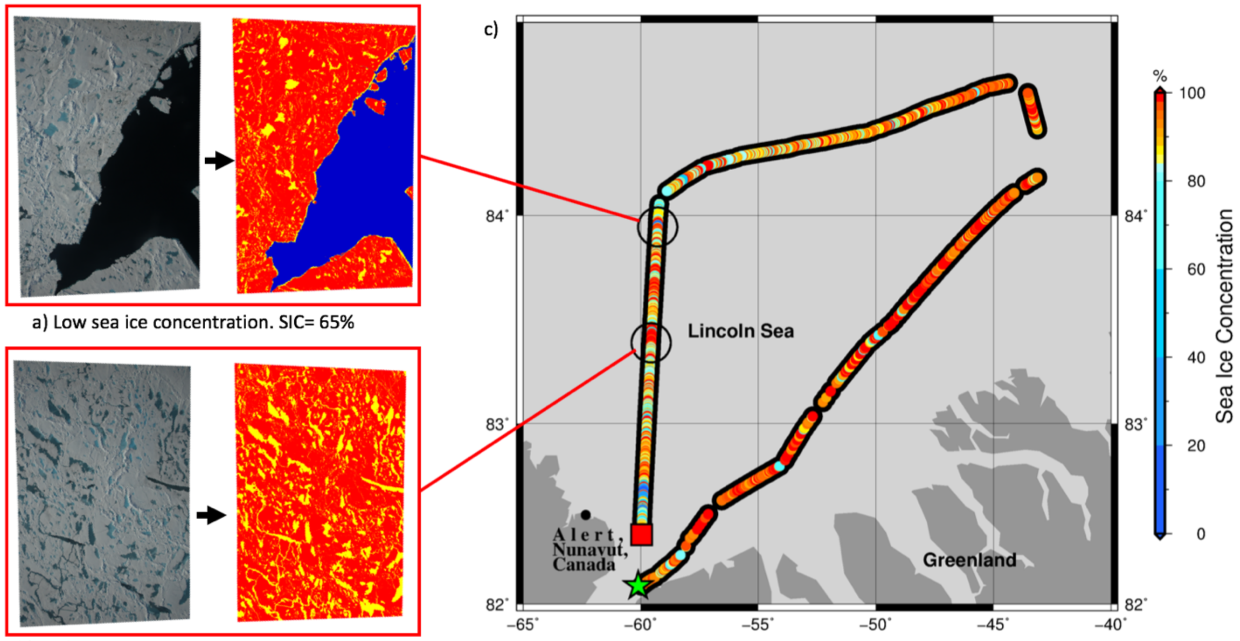

a) Low sea ice concentration. SIC= 65%

b) High sea ice concentration. SIC= 100%

Figure 11. *Map of sea ice concentration values per image along the flight line. (a) example of a DMS image with relatively low sea ice concentration compared with (b0 an image showing high sea ice concentration. (c) the calculated sea ice concentration along the survey line. The green star indicates the start of the flight, and the red square indicates the end of the survey on 24 July, 2017.*

Ice concentration is high throughout the survey, especially in the area closest to the Greenland coast. The high resolution of the DMS images allows for areas with open water to be resolved. For example, Figure 11a shows the algorithm effectively classifying an image with sea ice concentration of 65 %, a low value for this area. Figure 11b shows 100 % sea ice concentration with many light melt ponds. The color bar used for Figure 11b finely discretizes the values from 80-100% in order to distinguish between values, as most ice concentration values along this survey line are in this range.

Figure 12 shows visible satellite imagery and the ice concentration product for comparison with results from this study. In Figure 12a, the Moderate Resolution Imaging Spectroradiometer (MODIS) true color corrected reflectance shows the natural color imagery of the study area on 24 July, 2017. Figure 12b shows 12.5 km resolution Sea Ice Concentration derived from the Advanced Microwave Scanning Radiometer 2 (AMSR2) for 24 July, 2017 (Meier et al. 2018). Both images show very high ice concentration. The sea ice concentration values throughout most of Figure 12b are light pink and white indicating an ice concentration greater than 90%. The exception is to the east of Alert, Nunavut, Canada, where there is lower sea ice concentration. Figure 12a validates the satellite-derived ice concentration, showing large areas of open water in this region. This is also consistent with the lower ice concentration values found in this study at this location after applying our classification algorithm to the DMS images (Figure 11c).

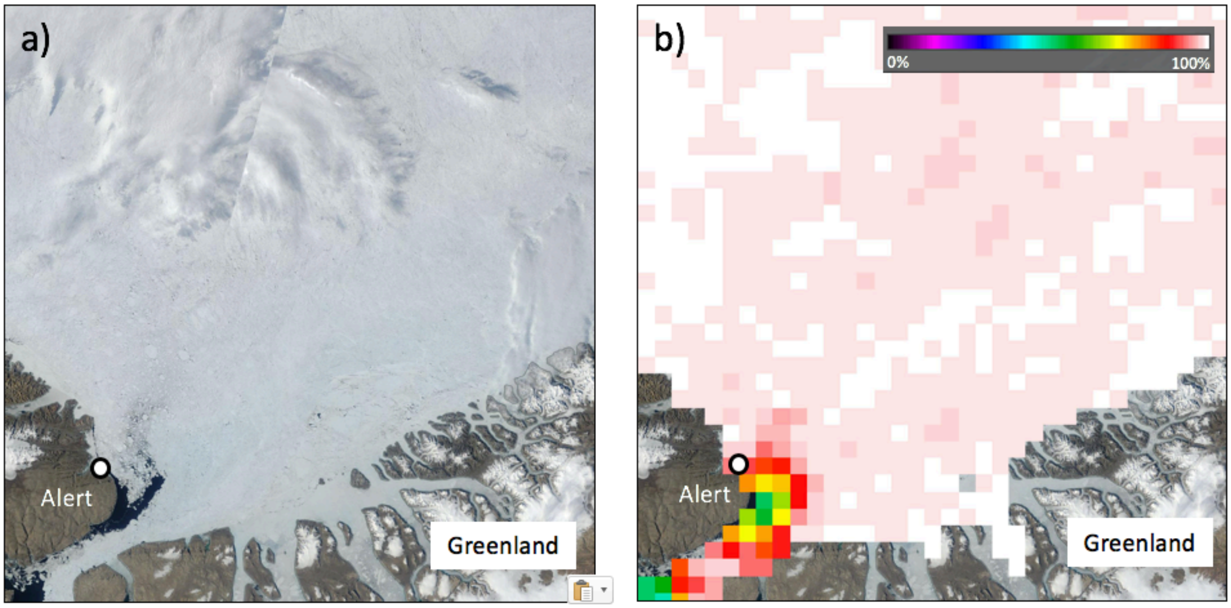

Figure 12. *Comparison of visible imagery and ice concentration in the study area on 24 July, 2017.*(a*) MODIS corrected reflection natural color imagery with 1-day temporal resolution and 250 m spatial resolution. (b) The 12.5 km AMSR2 sea ice concentration daily composite.*

It is important to note that the AMSR2 Sea Ice Concentration data are at 12.5 km x 12.5 km resolution, more than 600 times lower resolution than the ice concentration parameter derived from the DMS surface classification (recall DMS images are approximately 400 m x 575 m). Therefore, the lower-resolution satellite-derived ice concentration product cannot distinguish small areas of open water and variability, while the DMS derived product can resolve such features. We find a wider range of ice concentration values (2 %-100 %) because the higher resolution allows for larger percentages of open water per image.

4.4 Melt Pond Fraction

In addition to sea ice concentration, we calculate melt pond fraction along the survey line (Figure 13).

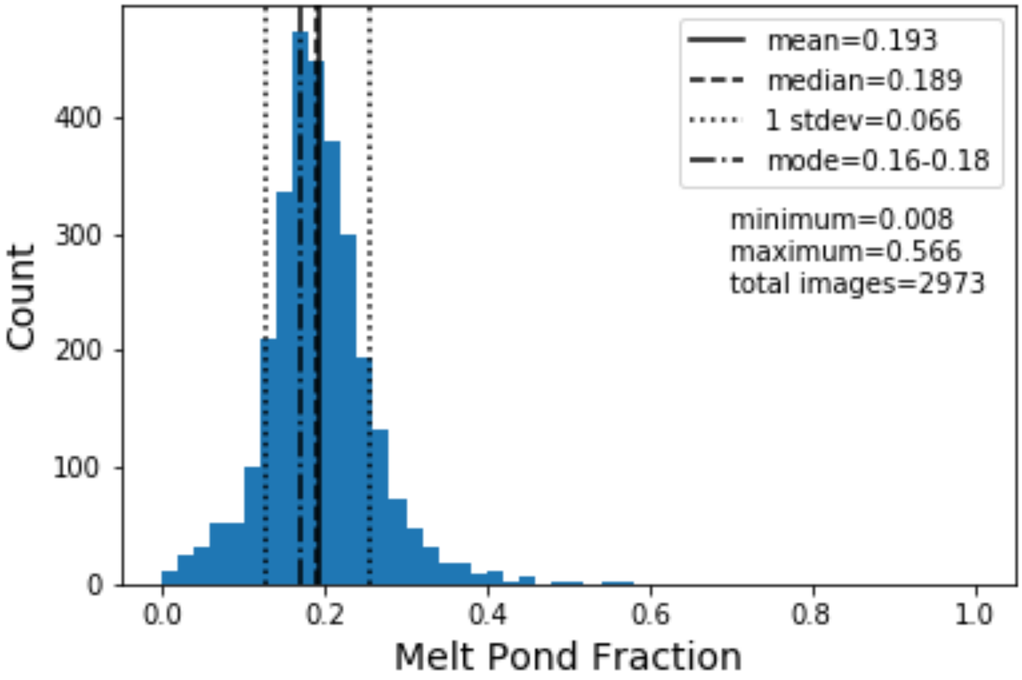

Figure 13. *Histogram of melt pond fraction calculated per image along the survey line flown on 24 July, 2017 over the Lincoln Sea. The bin width is 0.02. The resolution is ~400 m x ~575 m (0.23 km^2).*

The mean melt pond fraction is 0.19 with a standard deviation of 0.07. The median melt pond fraction is 0.19. The closeness of the median and mean fraction suggest it is an approximately normal distribution. The right tail indicates that there are some images with high melt pond fraction (up to 0.56) (Figure 14b). The melt pond fraction on multiyear ice compares favorably with previous studies (Webster et al. 2015, Perovich et al. 2002b). Webster et al. (2015) found a maximum average pond fraction of 0.38 on 23 July, 2011 in their study area on multiyear ice in the Beaufort Sea. Our findings show a lower melt pond fraction and we hypothesize that this is because the ice in our study area north of Greenland and the Canadian Archipelago is the thickest and most deformed sea ice in the Arctic, which restricts the lateral spread of melt ponds, resulting in a lower areal coverage. Figure 14 shows melt pond fraction and examples of images with high and low melt pond fractions.

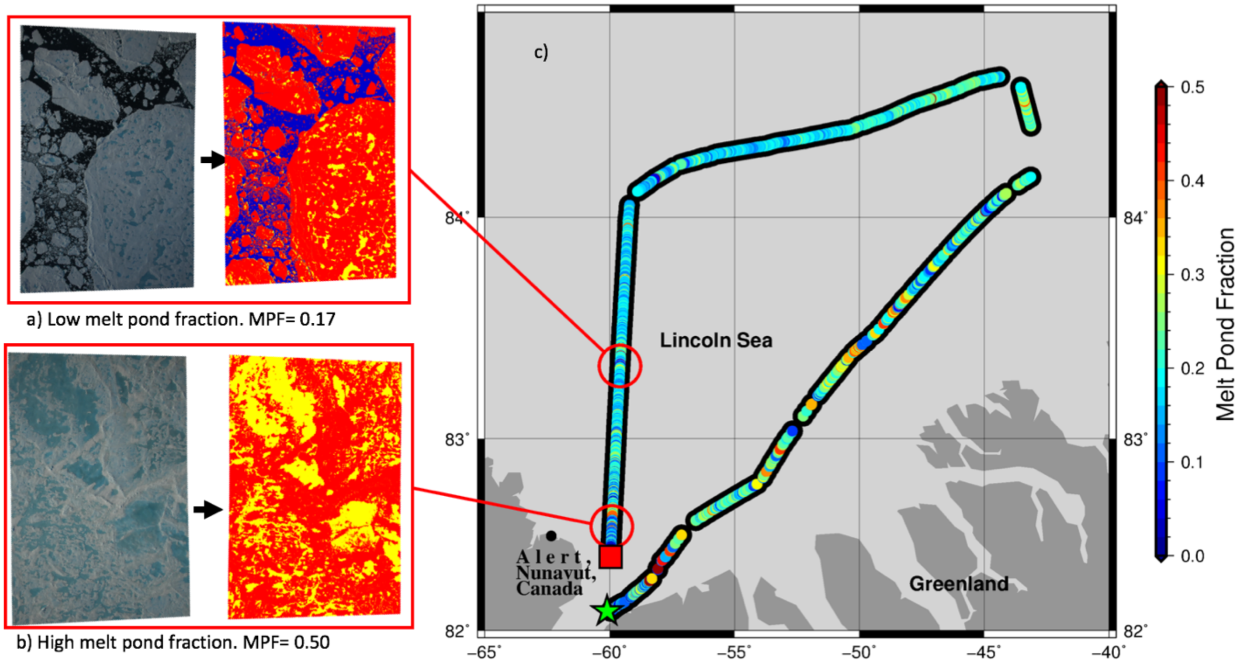
a) Low melt pond fraction. MPF= 0.17

b) High melt pond fraction. MPF= 0.50

***Figure 14**. Map of melt pond fraction per image along the 24 July, 2017 flight line. (a) example of an image with relatively low melt pond fraction (17%). (b) example of image with high melt pond fraction due to several large light melt ponds in the image area. (c) shows the calculated melt pond fraction along the survey line. The green star indicates the start of the flight, and the red square indicates the end of the survey.*

The highest variability of MPF is at the beginning of the survey line, north of Greenland. Melt ponds can occupy a large fraction of the image as seen in Figure 14b. Here the large pond in the upper left of the image is not able to drain through the thick multiyear ice and lateral spreading occurred across the relatively undeformed surface until a ridge was encountered.

4.5 Errors and Assumptions

In this section, we consider error and biases introduced during the data quality control step and the classification algorithm. We discuss the issues discovered in some images when visually inspecting the classification of images with unphysical or unrealistic results. We also discuss the common pixel misclassifications, consider potential limitations associated with the current version of the surface classification algorithm, and identify potential mechanisms for improvement. We comment on the tradeoff between algorithm accuracy and processing time tradeoffs. Some errors may require complicated steps to fix, while others require small algorithm adjustments that do not significantly increase the processing time.

4.5.1 Data Quality Control Errors and Biases

The filtering of data may introduce some statistical biases to the processed dataset. In some cases, the aircraft maneuvers (altering pitch and roll from the nominal settings) to avoid clouds. The images captured during this time may be discarded due to pitch and roll limitations or cloud obstruction. Clouds and sea smoke may preferentially form over areas over open water with a lower ice centration, due to abundance of available moisture. Therefore, discarding data with clouds may bias the dataset towards a conclusion of anomalously high sea ice concentration that does not capture the full reality of the amount of open water.

4.5.2 Algorithm Failures

During the image preprocessing and surface feature classification steps, we flagged all results that suggested the algorithm did not perform as intended. There are ~23 million surface pixels per image, with low variation (standard deviation ~30,000 pixels). We flagged images with fewer than 22.75 million surface pixels classified images with greater than 23.25 million pixels classified as surface. Upon inspecting these images, we found a number of images that contained open water were identified as border pixels rather than open water, resulting in too few surface pixels. This failure can be traced to the second step of the border finding methodology (Figure 5c). In this step the pixels less than Cb_mi_1 are classified as border pixels. If the open water pixels and border pixels occupy one mode (Cb_ma_1), when the mode is classified as border pixels, the open water pixels in that mode are also classified as border pixels. A solution to this misclassification would be to identify the width or pixel count of Cb_ma_1 and use these parameters to determine if the mode contains open water pixels. If the mode does contain open water pixels, we can use only the first step of the border classification step to identify border pixels.

Melt pond fraction was also an indicator of algorithm failure. Melt ponds pixels are defined as all unclassified pixels after the open water classification, so we used the melt pond fraction parameter to identify images where pixels were not appropriately classified by the algorithm. Previous studies have found maximum melt pond fractions on multiyear ice up to ~40% (Perovich et al. 2002a). We flagged images with melt pond fraction greater than 40% and visually inspected them to determine if these image classifications were accurate. In some images, a large section is classified as melt pond. This is due to overhead clouds that cast shadows on the surface and result in an image not being uniformly lit. This results in the shadowed part of the ice or the not-shadowed part of the open water to be classified as melt pond pixels. To resolve this issue, we can be more stringent with the manual filtering of images and to not only remove images with clouds obscuring the surface, but with overhead clouds casting shadows on parts of the image. The images that are fully in cloud shadows did not have this issue. Also, in some images, all of the surface pixels were classified as melt ponds. This is due to an error in the ice classification step that does not account for only one Cr mode. This step will be adjusted to account for this issue prior to running the algorithm on other flights.

In all, the algorithm failed on 203 images out of the 3,176, resulting in 2,973 (93.6%) of the quality images successfully analyzed. We have identified these failures and plan to modify the algorithm prior to processing the rest of the dataset.

4.5.3 Algorithm Misclassifications

The blurred RGB spaces of certain features results in misclassification of pixels. Arctic landscapes exhibit blue hues, with some features blended in the RGB space. Ice submerged in water generally has a light blue color. The only category related to submerged ice is the melt pond category, resulting in many types of submerged ice being misclassified as melt ponds. False positive melt pond misclassifications include brash ice draft between ice floes and ice floe edges. Submerged ice pixels, whether melt pond or ice edge draft, have the same RGB values and therefore we are not able to adjust this pixel-based, RGB-sensitive, algorithm to distinguish between these features.

Ridge shadows on ice have a similar color intensity as melt ponds. They do exhibit a higher red value relative to the green and blue values compared to melt ponds and thus are separated from light melt ponds pixels in the algorithm (Figure 6e). However, some ridge shadows are classified as melt ponds. Due to ridge shadow adjacency to the bright deformed ice pressure ridges, we considered developing a shadow identification technique as previous studies have proven to be useful for various reasons (Webster et al. 2015, Duncan et al. 2018). However, snow blowing across a deformed ice floe will settle when it encounters an obstacle such as a pressure ridge. Therefore, melt pond formation adjacent to pressure ridges is common. Brightening dark surfaces next to pressure ridges could result in misclassifying melt pond pixels as ice pixels. The results show that on average, heavily deformed ice makes up less than 1% of the image surface, whereas melt pond pixels make up 13% of the surface on average. This information, in conjunction with manual inspection of DMS imagery, led us to conclude that ridge shadow misclassification is less significant and less common than the potential melt pond misclassification as sea ice. Without a shadow brightening technique implemented, we must note that there are some ridge shadows misclassified as melt ponds.

In addition to the misclassification occurring in the middle of the spectrum, at the high end of the intensity spectrum, sun glints in water are classified as ice. In areas with open water, the wind driven wave action results in a surface disturbance. When sunlight reflects off this disturbance, it can result in a specular reflection into the camera lens which saturates the pixel RGB values. In our current algorithm, white pixels resulting from sun glint are misclassified as ice. To mitigate this issue, we could identify small areas of ice pixels (e.g., 10 or fewer contiguous pixels classified as ice) that are surrounded by open water and reclassify these areas as open water. Wave action, and thus the occurrence of sun glints, is most prevalent in areas with a large fetch of open water, so it may only be necessary to account for sun glints on images with a high open water fraction.

Grouping of pixels into objects and considering geometric thresholding may improve the accuracy of classification and resolve some of the aforementioned misclassification errors. However, these methods would likely significantly increase computational time and could result in additional, unforeseen errors.

Chapter 5: Summary and Conclusions

We have demonstrated the ability to effectively classify summer sea ice features in DMS imagery. We described a new algorithm to classify sea ice features into undeformed sea ice, deformed sea ice, melt ponds and open water categories. In addition, we derive meaningful sea ice parameters from the statistics of the classified surface features including SIC and MPF. The sea ice concentration values compare favorably with established products, although demonstrate the limitations of low-resolution, satellite-derived products. The mean sea ice concentration was 90.2 % with a standard deviation of 11.1 %. The melt pond fractions derived in this study are comparable to known values. On average, the melt pond fraction was 19.3 % with a standard deviation of 6.5 %. This study acts as a proof of concept and demonstrates the feasibility of classifying sea ice features.

These preliminary results justify further analysis of the remaining Arctic sea ice summer IceBridge flights. Next steps include processing the data acquired during the remaining five flights from 2016 and five flights from 2017. This will allow us to examine the differences in melt pond parameters across first year and multiyear ice more thoroughly and draw conclusions about Arctic wide melt pond coverage. We will also analyze melt pond areal details such as melt pond size and distribution. Melt pond appearance, size, and distribution are dependent on the thickness and surface topography of the ice (Eicken et al. 2004), and well as the snow distribution (Polashenski et al. 2012). With the coincident measurements of surface topography by the Airborne Topographic Mapper (ATM) (Studinger 2013), we can evaluate the relationship between topography and melt pond distribution. We can investigate the relationship between thickness, melt pond color, and snow depth at the end of winter (Newman et al. 2014; Blanchard-

Wrigglesworth et al. 2018) to evaluate relationships between end of winter sea ice properties and the summer distribution and melt pond location and size.

Our classification methodology may be applied to other high-resolution natural color imagery. With the possibility of analyzing datasets that span multiple years and various regions, there is potential for drawing conclusions about melt pond fraction variability and trends. Such a product would enhance our understanding of melt ponds coverage across the Arctic and provide information to the sea ice modeling community that may better inform sea ice forecasting efforts. We will derive an ice concentration product that may be used to validate the lower resolution satellite-derived products. All data products created in future work will be publicly available for use in the sea ice community.

Efforts to understand the melt season and improve modeling accuracy are especially important in the context of the changing Arctic. With a transition from multiyear ice to predominantly first year ice, we expect to see changes in melt pond areal coverage and characteristics. Understanding relationships between ice type, surface topography, snow, and melt pond coverage can allow us to better predict future melt pond conditions and forecast summer sea ice extent.

References

Arrigo, K. R., and Coauthors, 2012: Massive phytoplankton blooms under arctic sea ice. *Science,* **336**, 1408, doi:10.1126/science.1215065.

Blanchard-Wrigglesworth, E., M. A. Webster, S. L. Farrell, and C. M. Bitz, 2018: Reconstruction of Snow on Arctic Sea Ice. *J. Geophys. Res. Ocean.*, **123**, 3588–3602, doi:10.1002/2017JC013364.

Boisvert, L. N., T. Markus, and T. Vihma, 2013: Moisture flux changes and trends for the entire Arctic in 2003-2011 derived from EOS Aqua data. *J. Geophys. Res. Ocean.*, **118**, 5829–5843, doi:10.1002/jgrc.20414.

Clark, P. U., N. G. Pisias, T. F. Stocker, and A. J. Weaver, 2002: The role of the thermohaline circulation in abrupt climate change. *Nature,* **415**, 863–869, doi:10.1007/978-3-319-90975-2_4.

Comiso, J. C., 2012: Large Decadal Decline of the Arctic Multiyear Ice Cover. *J. Clim.*, **25**, 1176–1193, doi:10.1175/JCLI-D-11-00113.1.

Comiso, J. C., C. L. Parkinson, R. Gersten, and L. Stock, 2008: Accelerated decline in the Arctic sea ice cover. *Geophys. Res. Lett.*, **35**, 1–6, doi:10.1029/2007GL031972.

Crittenden, L., 2017: OIB-HU-25A Guardian #524 07/24/17 Science Report. https://espo.nasa.gov/oib/flight_reports/HU-25A_Guardian_524_07_24_17

Curry, J. A., J. L. Schramm, D. K. Perovich, and J. O. Pinto, 2001: Applications of SHEBA/FIRE data to evaluation of snow/ice albedo parameterizations. *J. Geophys. Res. Atmos.*, **106**, 15345–15355, doi:10.1029/2000JD900311.

Curry, J. A., J. L. Schramm, E. E. Ebert, 1995: Sea Ice-Albedo Climate Feedback Mechanism. *J. Clim.*, **8**, 240–247, doi: *10.1175/1520-0442(1995)008<0240:SIACFM>2.0.CO;2*

Dominguez, R., IceBridge DMS L1B Geolocated and Orthorectified Images, Version 1. *Boulder, Color. USA. NASA Natl. Snow Ice Data Cent. Distrib. Act. Arch. Cent.*, doi: https://doi.org/10.5067/OZ6VNOPMPRJ0.

Duncan, K., S. L. Farrell, L. N. Connor, J. Richter-Menge, J. K. Hutchings, and R. Dominguez, 2018: High-resolution airborne observations of sea-ice pressure ridge sail height. *Ann. Glaciol.*, **59**, 137–147, doi:10.1017/aog.2018.2.

Eicken, H., T. C. Grenfell, D. K. Perovich, J. A. Richter-Menge, and K. Frey, 2004: Hydraulic controls of summer Arctic pack ice albedo. *J. Geophys. Res. C Ocean.*, **109**, 1–13, doi:10.1029/2003JC001989.

Farrell, S. L., T. Markus, R. Kwok, and L. Connor, 2011: Laser altimetry sampling strategies over sea ice. *Ann. Glaciol.*, **52**, 69–76, doi:10.3189/172756411795931660.

Fetterer, F., and N. Untersteiner, 1998: Observations of melt ponds on Arctic sea ice. *J. Geophys. Res. Ocean.*, **103**, 24821–24835, doi:10.1029/98JC02034.

Fetterer, F., K. Knowles, W. N. Meier, M. Savoie, and A. K. Windnagel. 2017, updated daily. *Sea Ice Index, Version 3*. [Northern Hemisphere Monthly Data]. Boulder, Colorado USA. NSIDC: National Snow and Ice Data Center. doi: https://doi.org/10.7265/N5K072F8. [January 2019].

Flocco, D., D. L. Feltham, and A. K. Turner, 2010: Incorporation of a physically based melt pond scheme into the sea ice component of a climate model. *J. Geophys. Res.*, **115**, C08012, doi:10.1029/2009JC005568.

Flocco, D., D. Schröder, D. L. Feltham, and E. C. Hunke, 2012: Impact of melt ponds on Arctic sea ice simulations from 1990 to 2007. *J. Geophys. Res. Ocean.*, **117**, doi:10.1029/2012JC008195.

Francis, J. A., and S. J. Vavrus, 2015: Evidence for a wavier jet stream in response to rapid Arctic warming. *Environ. Res. Lett.*, **10**, doi:10.1088/1748-9326/10/1/014005.

Grenfell, T. C., and D. K. Perovich, 2004: Seasonal and spatial evolution of albedo in a snow-ice-land-ocean environment. *J. Geophys. Res.*, **109**, C01001, doi:10.1029/2003JC001866.

Haas, C., 2017: Sea ice thickness distribution, *Sea Ice*, David N. Thomas (Eds.), John Wiley & Sons, Ltd., 42-64.

Hunke, E. C., W. H. Lipscomb, and A. K. Turner, 2010: Sea-ice models for climate study: retrospective and new directions. **56**, 1162–1172, doi:10.3189/002214311796406095.

Intrieri, J. M., 2002: An annual cycle of Arctic surface cloud forcing at SHEBA. *J. Geophys. Res.*, **107**, 1–14, doi:10.1029/2000jc000439.

Istomina, L., and Coauthors, 2015: Melt pond fraction and spectral sea ice albedo retrieval from MERIS data - Part 1: Validation against in situ, aerial, and ship cruise data. *Cryosphere*, **9**, 1551–1566, doi:10.5194/tc-9-1551-2015.

Koenig, L. S., S. Martin, M. Stundinger, and J. Sonntag, 2010: polar Airborne Observations Fill Gap in Satellite Data. *Eos* (Washington DC)., **91**, 333-334

Krabill, W. B., W. Abdalati, E. B. Frederick, S. S. Manizade, C. F. Martin, J. G. Sonntag, R. N. Swift, R. H. Thomas, and J. G. Yungel, 2002: Aircraft laser altimetry measurement of elevation changes of the Greenland ice sheet: Technique and accuracy assessment. *J. Geodynamics*, vol. **34** no. 3/4, 357–376

Kurtz, N. T., and Coauthors, 2013: Sea ice thickness, freeboard, and snow depth products from Operation IceBridge airborne data. *Cryosphere*, **7**, 1035–1056, doi:10.5194/tc-7-1035-2013.

Kwok, R., and D. A. Rothrock, 2009: Decline in Arctic sea ice thickness from submarine and ICESat records: 1958-2008. *Geophys. Res. Lett.*, **36**, doi:10.1029/2009GL039035.

Kwok, R., 2005: Variability of Nares Strait ice flux. *Geophys. Res. Lett.*, **32**, 1–4, doi:10.1029/2005GL024768.

Kwok, R., 2015: Sea ice convergence along the Arctic coasts of Greenland and the Canadian Arctic Archipelago: Variability and extremes (1992-2014). *Geophys. Res. Lett.*, **42**, 7598–7605, doi:10.1002/2015GL065462.

Laxon, S. W., and Coauthors, 2013: CryoSat-2 estimates of Arctic sea ice thickness and volume. *Geophys. Res. Lett.*, **40**, 732–737, doi:10.1002/grl.50193.

Lu, P., M. Leppäranta, B. Cheng, Z. Li, L. Istomina, and G. Heygster, 2018: The color of melt ponds on Arctic sea ice. *Cryosphere*, **12**, 1331–1345, doi:10.5194/tc-12-1331-2018.

Mäkynen, M., S. Kern, A. Rösel, and L. T. Pedersen, 2014: On the estimation of melt pond fraction on the arctic sea ice with ENVISAT WSM images. *IEEE Trans. Geosci. Remote Sens.*, **52**, 7366–7379, doi:10.1109/TGRS.2014.2311476.

Markus, T., D. J. Cavalieri, and A. Ivanoff, 2002: The potential of using Landsat 7 ETM+ for the classification of sea-ice surface conditions during summer. *Ann. Glaciol.*, **34**, 415–419, doi:10.3189/172756402781817536.

Markus, T., D. J. Cavalieri, M. A. Tschudi, and A. Ivanoff, 2003: Comparison of aerial video and Landsat 7 data over ponded sea ice. *Remote Sens. Environ.*, **86**, 458–469, doi:10.1016/S0034-4257(03)00124-X.

Maykut, G. A., 1978: Energy Exchange Over Young Sea Ice in the Central Arctic. *J. Geophys. Res. C Ocean.,* 83, 3646–3658. 10.1029/JC083iC07p03646

Meier, W. N., T. Markus, and J. C. Comiso. 2018. *AMSR-E/AMSR2 Unified L3 Daily 12.5 km Brightness Temperatures, Sea Ice Concentration, Motion & Snow Depth Polar Grids, Version 1*. Boulder, Colorado USA. NASA National Snow and Ice Data Center Distributed Active Archive Center. doi: https://doi.org/10.5067/RA1MIJOYPK3P. [8 May, 2019].

Miao, X., H. Xie, S. F. Ackley, D. K. Perovich, and C. Ke, 2015: Object-based detection of Arctic sea ice and melt ponds using high spatial resolution aerial photographs. *Cold Reg. Sci. Technol.*, **119**, 211–222, doi:10.1016/j.coldregions.2015.06.014.

Newman, T., S. L. Farrell, J. Richter-Menge, L. N. Connor, N. T. Kurtz, B. C. Elder, and D. McAdoo, 2014: Assessment of radar-derived snow depth over Arctic sea ice. *J. Geophys. Res. C Ocean.*, doi:10.1002/2014JC010284.

Onana, V.-D.-P., N. T. Kurtz, S. L. Farrell, L. S. Koenig, M. Studinger, and J. P. Harbeck, 2013: A Sea-Ice Lead Detection Algorithm for Use With High-Resolution Airborne Visible Imagery. *IEEE Trans. Geosci. Remote Sens.*, **51**, 38–56, doi:10.1109/TGRS.2012.2202666.

Osborne, E., J. Richter-Menge, and M. Jeffries, Eds., 2018: Arctic Report Card 2018. https://www.arctic.noaa.gov/Report-Card

Panzer, B., D. Gomez-Garcia, C. Leuschen, J. Paden, F. Rodriguez-Morales, A. Patel, T. Markus, B. Holt, and P. Gogineni, 2013: An ultra-wideband, microwave radar for measuring snow thickness on sea ice and mapping near-surface internal layers in polar firn, *J. Glaciol.*, **59**, 244–254, doi:10.3189/2013JoG12J128.

Perovich, D. K., T. C. Grenfell, B. Light, and P. V. Hobbs, 2002a: Seasonal evolution of the albedo of multiyear Arctic sea ice. *J. Geophys. Res.*, **107**, 8044, doi:10.1029/2000JC000438.

Perovich, D. K., 2002b: Aerial observations of the evolution of ice surface conditions during summer. *J. Geophys. Res.*, **107**, 8048, doi:10.1029/2000JC000449.

Perovich, D., 2011: The Changing Arctic Sea Ice Cover. *Oceanography*, **24**, 162–173, doi:10.5670/oceanog.2011.68.

Perovich, D. K., and C. Polashenski, 2012: Albedo evolution of seasonal Arctic sea ice. *Geophys. Res. Lett.*, **39**, 1–6, doi:10.1029/2012GL051432.

Perovich, D.K., 2017, Sea ice and sunlight, *Sea Ice*, David N. Thomas (Eds.), John Wiley & Sons, Ltd., 110-137.

Petrich, C., H. Eicken, C. M. Polashenski, M. Sturm, J. P. Harbeck, D. K. Perovich, and D. C. Finnegan, 2012: Snow dunes: A controlling factor of melt pond distribution on Arctic sea ice. *J. Geophys. Res. Ocean.*, **117**, doi:10.1029/2012JC008192.

Polashenski, C., D. Perovich, and Z. Courville, 2012: The mechanisms of sea ice melt pond formation and evolution. *J. Geophys. Res. Ocean.*, **117**, 1–23, doi:10.1029/2011JC007231.

Rösel, A., L. Kaleschke, and G. Birnbaum, 2012: Melt ponds on Arctic sea ice determined from MODIS satellite data using an artificial neural network. *Cryosphere*, **6**, 431–446, doi:10.5194/tc-6-431-2012.

Rösel, A., and L. Kaleschke, 2011: Comparison of different retrieval techniques for melt ponds on Arctic sea ice from Landsat and MODIS satellite data. *Ann. Glaciol.*, **52**, 185–191, doi:10.3189/172756411795931606.

Rösel, A., and L. Kaleschke, 2012: Exceptional melt pond occurrence in the years 2007 and 2011 on the Arctic sea ice revealed from MODIS satellite data. *J. Geophys. Res. Ocean.*, **117**, 1–9, doi:10.1029/2011JC007869.

Schröder, D., D. L. Feltham, D. Flocco, and M. Tsamados, 2014: September Arctic sea-ice minimum predicted by spring melt-pond fraction. *Nat. Clim. Chang.*, **4**, 353–357, doi:10.1038/nclimate2203.

Screen, J. A., and I. Simmonds, 2010: The central role of diminishing sea ice in recent Arctic temperature amplification. *Nature*, **464**, 1334. https://doi.org/10.1038/nature09051.

Studinger, Michael, D. Young, and C. Larsen, 2011: *IceBridge Mission Flight Reports, Version 1*. [Subsets: 2016_GR_NASA, 2017_GR_NASA] Boulder, Colorado USA. NASA National Snow and Ice Data Center Distributed Active Archive Center.

Studinger, M. 2013, updated 2018. *IceBridge ATM L1B Elevation and Return Strength, Version 2*. Boulder, Colorado USA. NASA National Snow and Ice Data Center Distributed Active Archive Center. doi: https://doi.org/10.5067/19SIM5TXKPGT.

Tschudi, M. A., J. A. Curry, and J. A. Maslanik, 2001: Airborne observations of summertime surface features and their effect on surface albedo during FIRE/SHEBA. *J. Geophys. Res. Atmos.*, **106**, 15335–15344, doi:10.1029/2000JD900275

Tschudi, M. A., J. A. Maslanik, and D. K. Perovich, 2008: Derivation of melt pond coverage on Arctic sea ice using MODIS observations. *Remote Sens. Environ.*, **112**, 2605–2614, doi:10.1016/j.rse.2007.12.009.

Uttal, T., and Coauthors, 2002: Surface Heat Budget of the Arctic Ocean. *Bull. Am. Meteorol. Soc.*, **83**, 255–275, doi:10.1175/1520-0477(2002)083<0255:shbota>2.3.co;2.

Webster, M. A., I. G. Rigor, D. K. Perovich, J. A. Richter-Menge, C. M. Polashenski, and B. Light, 2015: Seasonal evolution of melt ponds on Arctic sea ice. *J. Geophys. Res. Ocean.*, **120**, 1–15, doi:10.1002/2015JC011030.

World Meteorological Organization (WMO), 1970: Sea ice nomenclature, WMO/OMM/BMO Rep. 259, Geneva.

Wright, N. C., and C. M. Polashenski, 2018: Open-source algorithm for detecting sea ice surface features in high-resolution optical imagery. *Cryosphere*, **12**, 1307–1329, doi:10.5194/tc-12-1307-2018.

Zege, E., A. Malinka, I. Katsev, A. Prikhach, G. Heygster, L. Istomina, G. Birnbaum, and P. Schwarz, 2015: Algorithm to retrieve the melt pond fraction and the spectral albedo of Arctic summer ice from satellite optical data. *Remote Sens. Environ.*, **163**, 153–164, doi:10.1016/j.rse.2015.03.012.